Roman Warm Period and Late Antique Little Ice Age in an Earth System Model Large Ensemble

Feng Shi, Cheng Sun, Antoine Guion, Qiuzhen Yin, Sen Zhao, Ting Liu, Zhengtang Guo

JGR Atmospheres

RESEARCH ARTICLE
10.1029/2021JD035832

Roman Warm Period and Late Antique Little Ice Age in an Earth System Model Large Ensemble

Feng Shi[1,2], Cheng Sun[3], Antoine Guion[4,5], Qiuzhen Yin[5], Sen Zhao[6,7], Ting Liu[8,9], and Zhengtang Guo[1,2,10]

[1]Key Laboratory of Cenozoic Geology and Environment, Institute of Geology and Geophysics, Chinese Academy of Sciences, Beijing, China, [2]Center for Excellence in Life and Paleoenvironment, Chinese Academy of Sciences, Beijing, China, [3]College of Global Change and Earth System Science (GCESS), Beijing Normal University, Beijing, China, [4]LMD/IPSL, Sorbonne Université, ENS, PSL Université, École polytechnique, Institut Polytechnique de Paris, CNRS, Paris, France, [5]Georges Lemaître Centre for Earth and Climate Research, Earth and Life Institute, Université Catholique de Louvain, Louvain-la-Neuve, Belgium, [6]CIC-FEMD/ILCEC, Key Laboratory of Meteorological Disaster of Ministry of Education, College of Atmospheric Sciences, Nanjing University of Information Science and Technology, Nanjing, China, [7]Department of Atmospheric Sciences, University of Hawaii at Mānoa, Honolulu, HI, USA, [8]State Key Laboratory of Satellite Ocean Environment Dynamics, Second Institute of Oceanography, Ministry of Natural Resources, Hangzhou, China, [9]Southern Marine Science and Engineering Guangdong Laboratory (Zhuhai), Zhuhai, China, [10]University of Chinese Academy of Sciences, Beijing, China

Abstract Changes in climate during the Roman Warm Period (RWP, 1–250 CE) and Late Antique Little Ice Age (LALIA, 536–660 CE) play a critical role in early societal evolution, but the climate differences between these two periods and the possible causes of the changes remain poorly explored. Here we use the LOch–Vecode-Ecbilt-CLio-agIsM model Large Common Era Ensemble with 70 members to examine the climate change over these two intervals and compare the results of this ensemble with the latest temperature reconstructions from the Past Global Changes 2k network and the transient simulation for the past 2,000 years from the Community Earth System Model. Results from both proxy reconstructions and climate model simulations show warming in mid-to-high latitudes of the Northern Hemisphere (NH) during the RWP compared with the LALIA. This is likely linked with the increased radiative forcing associated with weaker volcanic eruptions in the RWP, which results in reduced sea ice area and pronounced high-latitude warming through surface albedo and lapse-rate feedbacks. This increases the upper ocean heat content over centennial time scales to maintain warming over the NH high-latitude regions. Moreover, the RWP has drier (wetter) conditions in the eastern (western) equatorial Pacific than the LALIA, and this is related to the zonal sea surface temperature gradient in the equatorial Pacific through modification of the zonal circulation.

Plain Language Summary Climate changes during the Roman Warm Period (RWP) and Late Antique Little Ice Age (LALIA) had large impacts on human migration, agricultural production, and political upheaval. However, little is known about the mechanism of climate change during these periods. We analyze the climate differences during the two periods using large ensemble climate model simulations and the latest proxy reconstructions. We find two consistent dominant features from model–data comparison: warming in mid-to-high latitudes of the Northern Hemisphere (NH) and drier (wetter) precipitation anomalies in the eastern (western) equatorial Pacific in the RWP than in the LALIA. Mid-to-high latitude warming may be related to the increased radiative forcing associated with weaker volcanic eruptions in the RWP, resulting in the decrease of sea ice area and Arctic warming amplification through positive surface albedo and lapse-rate feedbacks. The precipitation differences may be caused by modification of the zonal circulation, which is forced by the atmosphere–ocean interaction in the tropical Pacific. These mechanisms of climate change during the RWP and LALIA periods had not been identified through model–data comparison previously.

Key Points:

- Roman Warm Period (RWP) was warmer than the Late Antique Little Ice Age (LALIA) in the mid-high latitudes of the Northern Hemisphere (NH)
- Large ensemble modeling shows the climate difference between the RWP and LALIA exceeds the internal variability of the climate system
- The temperature change over the NH is linked to volcanic activity mainly through surface albedo and lapse-rate feedback

Supporting Information:

Supporting Information may be found in the online version of this article.

Correspondence to:

F. Shi,
shifeng@mail.iggcas.ac.cn

Citation:

Shi, F., Sun, C., Guion, A., Yin, Q., Zhao, S., Liu, T., & Guo, Z. (2022). Roman Warm Period and Late Antique Little Ice Age in an Earth System Model Large Ensemble. *Journal of Geophysical Research: Atmospheres*, *127*, e2021JD035832. https://doi.org/10.1029/2021JD035832

Received 8 SEP 2021
Accepted 23 JUL 2022

Author Contributions:

Conceptualization: Feng Shi
Data curation: Feng Shi, Antoine Guion
Formal analysis: Feng Shi, Cheng Sun, Sen Zhao, Ting Liu
Funding acquisition: Feng Shi, Zhengtang Guo
Methodology: Feng Shi, Antoine Guion
Project Administration: Feng Shi, Zhengtang Guo
Resources: Feng Shi, Qiuzhen Yin, Zhengtang Guo
Visualization: Feng Shi, Sen Zhao, Ting Liu
Writing – original draft: Feng Shi
Writing – review & editing: Feng Shi, Cheng Sun, Antoine Guion, Qiuzhen Yin, Sen Zhao, Ting Liu

1. Introduction

The Roman Warm Period (RWP) and Late Antique Little Ice Age (LALIA) are two periods of remarkably strong climate anomalies during the first millennium of the Common Era (CE). Previous researches have suggested that the RWP was even warmer than the Medieval Climate Anomaly (MCA) and the Current Warm Period (CWP) (Bianchi & McCave, 1999; Keigwin, 1996). The RWP has been defined as the interval 1–300 CE from the

Northern Hemisphere (NH) temperature reconstruction (Ljungqvist, 2010), but the temperature during the period 251–300 CE was already relatively low. Thus, we define the RWP as 1–250 CE. The cold climate during the LALIA (536–660 CE) was defined by tree-ring chronologies in the Russian Altai and European Alps (Büntgen et al., 2016), and confirmed by an integrated tree-ring record in the Northern Hemisphere (Büntgen et al., 2020). Note that there is still some controversy about LALIA definition because some other types of proxy records indicate a longer cooling period known as the Dark Age Cold Period (400–765 CE; Helama et al. [2017]).

Climate change during the RWP and LALIA played a vital role in subsistence patterns and societal reorganization (Büntgen et al., 2016; T. Wang et al., 2013). However, less attention has been paid to these two periods than to the MCA and Little Ice Age (LIA) during the second millennium of the CE, as proxy records and climate model simulations for the RWP and LALIA are relatively scarce. Most proxy records focus on temperature reconstructions covering the first millennium of the CE (e.g., Helama et al., 2017). New temperature field reconstructions for the past two millennia based on unprecedented proxy records have provided an opportunity to examine the spatial patterns of these two periods (Neukom et al., 2019). However, there is a little reconstruction of other climate variables such as precipitation, sea ice, and atmospheric and oceanic circulation.

A time series comparison of the proxy record and external forcing suggests that the NH temperature change during LALIA was linked with volcanic forcing (Büntgen et al., 2016), and the variations in solar and volcanic forcing may be responsible for the reconstructed NH temperatures during the RWP (Büntgen et al., 2020; Ljungqvist, 2010). Numerous previous modeling studies have found and confirmed that volcanic eruptions dominated hemispheric temperature changes over the second millennium of the CE (Brönnimann et al., 2019; Crowley, 2000; Hegerl et al., 2003; Schneider et al., 2009; Schurer et al., 2014). Furthermore, the prominent role of volcanic eruptions in the sixth-century temperature was confirmed by climate model simulations (Toohey, Stevens, et al., 2016; van Dijk et al., 2022). However, the significant relationship between the solar activity and the NH temperature variability from the proxy data reconstructions (Connolly et al., 2021) is not supported by the climate model simulations over the second millennium of the CE (Schurer et al., 2014) and the Sun's total energy output measurement over the past 30 years (Foukal et al., 2006).

In fact, the climate feedback processes can amplify or weaken the influences of the natural external forcings on climate, but there is little evidence to quantify the physical feedbacks during the RWP and LALIA. Climate feedback is divided into two categories, radiative and non-radiative (Goosse et al., 2018). The key non-radiative feedbacks are mostly active over the Southern Ocean (Goosse et al., 2018). The major radiative feedbacks include the Planck, lapse rate, surface albedo, cloud, and water vapor feedbacks (Goosse et al., 2018; Previdi et al., 2021; Zhang et al., 1994). The amplitudes of the feedback are often quantified by a radiative feedback kernel method during the instrumental period (Soden & Held, 2006). The quantitative analysis of climate feedback is critical to advancing scientific understanding of the driving mechanisms of climate differences between the RWP and LALIA.

The Community Earth System Model (CESM), the most frequent full General Circulation Model (GCM), has been used to simulate the atmospheric, oceanic, and terrestrial feedbacks over the past two millennia, but the volcanic forcing only covers the last 1500 years due to the Gao et al. (2008)'s reconstruction limitation (Z. Wang et al., 2015; Yan et al., 2015). Volcanic aerosol data covering the past 2,000 years (Toohey & Sigl, 2016) were used in the CESM simulation (called CESM-past2k) (Zhong et al., 2018), which provides an opportunity to analyze the influences of the volcanic eruptions on climate differences during the RWP and LALIA. However, experiments performed with a single climate model cannot be used to isolate the uncertainty from model internal variability, which has substantial influence on simulated climate changes (Deser et al., 2020). Furthermore, the CESM Last Millennium Ensemble (LME) project (Otto-Bliesner et al., 2016) covers only the second millennium of the CE.

Here, we carry out 70 initial-condition ensemble simulations using the intermediate complexity Earth System Model (LOch–Vecode-Ecbilt-CLio-agIsm, LOVECLIM) under the same forcings scenario. This LOVECLIM Large Common Era Ensemble simulation is called LOVECLIM-LCE. The forced response from the LOVECLIM-LCE simulation can be estimated by averaging over enough members because the resulting sequences of unpredictable internal variability are phased randomly between the individual ensemble members and tend to cancel out (Deser et al., 2012). We then discuss the climate feedbacks and atmospheric circulation associated with the climate variation together with its possible origin, based on model–data comparison.

2. Data and Models

2.1. Data

Here, the instrumental temperature and precipitation data are taken from two datasets. The monthly global temperature observation dataset at 5.0° longitude × 5.0° latitude global grid from Hadley Center/Climatic Research Unit Temperature version 4.5 (HadCRUT4.5) (Morice et al., 2012). The monthly precipitation reanalysis dataset at a 1.0° latitude × 1.0° longitude global grid from the Twentieth Century Reanalysis version 3 (20CRv3), which is provided by the U.S. Department of Energy, Office of Science Biological and Environmental Research, by the National Oceanic and Atmospheric Administration (NOAA) Climate Program Office, and by the NOAA Physical Sciences Laboratory (Slivinski et al., 2019).

The latest six reconstructed global annual mean temperature anomaly field datasets (Neukom et al., 2019) were used for model–data comparison. These reconstructions are based on the most comprehensive and latest Past Global Changes 2k network (PAGES2k) temperature proxy dataset (PAGES2k Consortium, 2017). Six statistical reconstruction methods were used to reduce the influence of method selection on the reconstructions. Each method generates 100 ensemble members, resulting in a total ensemble size of 600. The ensemble perturbation in the first two methods (Composite plus scale and Principal-component regression) is achieved by adding noise time series with the same standard deviation of the residuals to each ensemble member (Neukom et al., 2019). The other four methods of producing members are more complicated; please refer to (Neukom et al., 2019) for details. In addition, there are six NH temperature reconstructions and one SH temperature reconstruction that have been published since 2014 CE, including the tree-ring reconstructions (Büntgen et al., 2021; Guillet et al., 2017; L. Schneider et al., 2015; Shi et al., 2015; Wilson et al., 2016) and the multi-proxy reconstruction (Neukom et al., 2014) to compare with the PAGES2k temperature reconstructions.

Global precipitation reconstruction is limited by low spatial coherency and the scarcity of precipitation-sensitive proxies. Here, only a data-assimilation-based annual precipitation rate at the surface from the Last Millennium Reanalysis (LMR) dataset is used for model–data comparison. It covers the past two millennia (1–2,000 CE) and is relatively credible, as proxy system models were used to account for seasonal responses of the proxy records, but the problem of scarce data in the first 700 years still exists in the LMR dataset (Tardif et al., 2019). The 20 ensemble members in the LMR dataset were generated through random drawings from the climate simulations and proxy reconstructions (Tardif et al., 2019).

2.2. Climate Models

The results of a transient simulation over the past 2 ka with the CESM version 1.1 (CESM-past2k) (Zhong et al., 2018) are used for model–data comparison. The horizontal resolution is 1.9° longitude × 2.5° latitude for the atmospheric component and 1° longitude × 1° latitude for the ocean.

It would be preferable to run a full GCM, but such a model is too computationally expensive to run in a large ensemble to obtain the probability distribution function of the outputs to investigate uncertainties in the climate model system. Thus, the intermediate complexity Earth System model LOVECLIM version 1.3 is used here, which is fully coupled with five different models: the atmospheric component, the ocean–sea ice component, the vegetation component, the ice sheets component, and the oceanic carbon cycle component (Goosse et al., 2010). The horizontal resolution is 5.6° longitude × 5.6° latitude for the atmospheric component and 3° longitude × 3° latitude for the ocean. The most important simplification in LOVECLIM is the intermediate complexity atmospheric component instead of a GCM, which saves considerable computing time (Goosse et al., 2010). This model provides an opportunity to perform a large simulation ensemble (Goosse et al., 2010), and has been verified as an adequate tool to reproduce the major characteristics of climate change over the last millennium (Goosse et al., 2006, 2012).

The experimental design refers to previous work (Guion, 2017) that was performed according to the protocol of the Paleoclimate Modeling Intercomparison Project Phase 4 (PMIP4) (Jungclaus et al., 2017). There are four major forcings: aerosols from volcanic eruptions, solar activity, greenhouse gases, and the orbital forcing over the past 2,000 years (Figure 1). The volcanic forcing has monthly resolution and is divided into four latitude bands (30°S–90°S, 0°S–30°S, 0°N–30°N, and 30°N–90°N; Figures 1a–1d). The volcanic reconstruction is from an ice-core-based volcanic stratospheric sulfur injection dataset named "eVolv2k_v1" (Toohey &

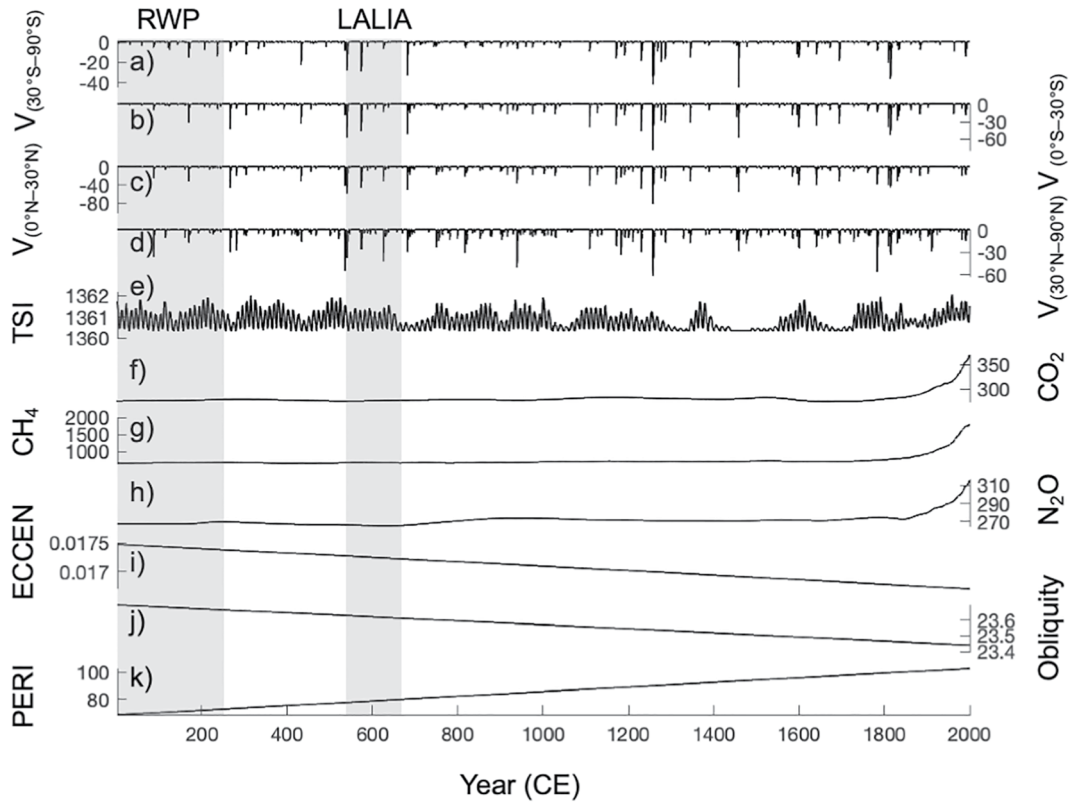

Figure 1. Evolution of the major forcings: (a) to (d) Volcanic aerosol forcing (V, unit: W m^{-2}) in four latitude bands; (e) Total solar irradiance (TSI, unit: W m^{-2}); (f) CO_2 (unit: ppm); (g) CH_4 (unit: ppb); (h) N_2O (unit: ppb); (i) Eccentricity of orbital ellipse (ECCEN, non-dimensional); (j) Latitude of Tropic of Cancer (Obliquity, unit: degree); and (k) Longitude of perihelion (PERI, unit: degree). Gray shaded bars indicate the RWP (1–250 CE) and LALIA (536–660 CE) periods.

Sigl, 2016). The aerosol optical depth (AOD) for visible light is first computed from the volcanic injections using the Easy Volcanic Aerosol (EVA) model, an idealized forcing generator for climate simulations (Toohey, Stevens, et al., 2016). The resulting AOD for the four bands of latitude is then multiplied by a factor of 4/0.7 to give the equivalent total solar irradiance (TSI), as suggested by Schmidt et al. (2011). This scaling applied to the TSI as a function of latitude (see Figures 1a–1d) is a much stronger simplification than in the CESM-past2k experiment, in which the stratospheric sulfate aerosol derived from the volcanic eruptions is distributed in the lower stratosphere (Zhong et al., 2018). Volcanic eruptions induce a negative signal on surface temperature through the scattering of incoming solar radiation by sulfate aerosols (Robock, 2000). The annual TSI anomalies with respect to the 1,360.8 W/m^2 during the historical period since 1850 CE is derived from Matthes et al. (2017), and before 1850 CE is calculated from the cosmogenic isotopes (Vieira et al., 2011) (Figure 1e). The three major components of the greenhouse gases (carbon dioxide, methane, and nitrous oxide, Figures 1f–1h) are from Meinshausen et al. (2017). The orbital forcing is the same for both PMIP3 and PMIP4 experiments and is based on the work of Berger (1978) (Figures 1j and 1k). The vegetation/land use forcing is from Lawrence et al. (2016) (data not shown).

Each member has been run for 1000 model years without any external forcing to reach a state of equilibrium. A small random perturbation is added to the sea surface temperature (SST) to generate 70 members with slightly different initial conditions but the same forcings. The global annual (April to March) SST for the 70 ensemble members over the first 1000 model years (the spin-up period) is shown in Figure 2a. There is a small mean standard deviation of 0.0407 °C and a small mean trend of 2.0952×10^{-4} °C per century over the last 500 model years (Figures 2b and 2c). Their ranges are 0.0380–0.0475 °C and -2.0001×10^{-5} to 7.9312×10^{-4} °C per century, respectively. This indicates that the climate drift of the LOVECLIM-LCE simulation is small, and the near-equilibrium ocean state taken as pre-industrial control simulation during the first 1000 model years is quite stable. These trends and standard deviations are smaller than those for most control runs of CMIP5 simulations

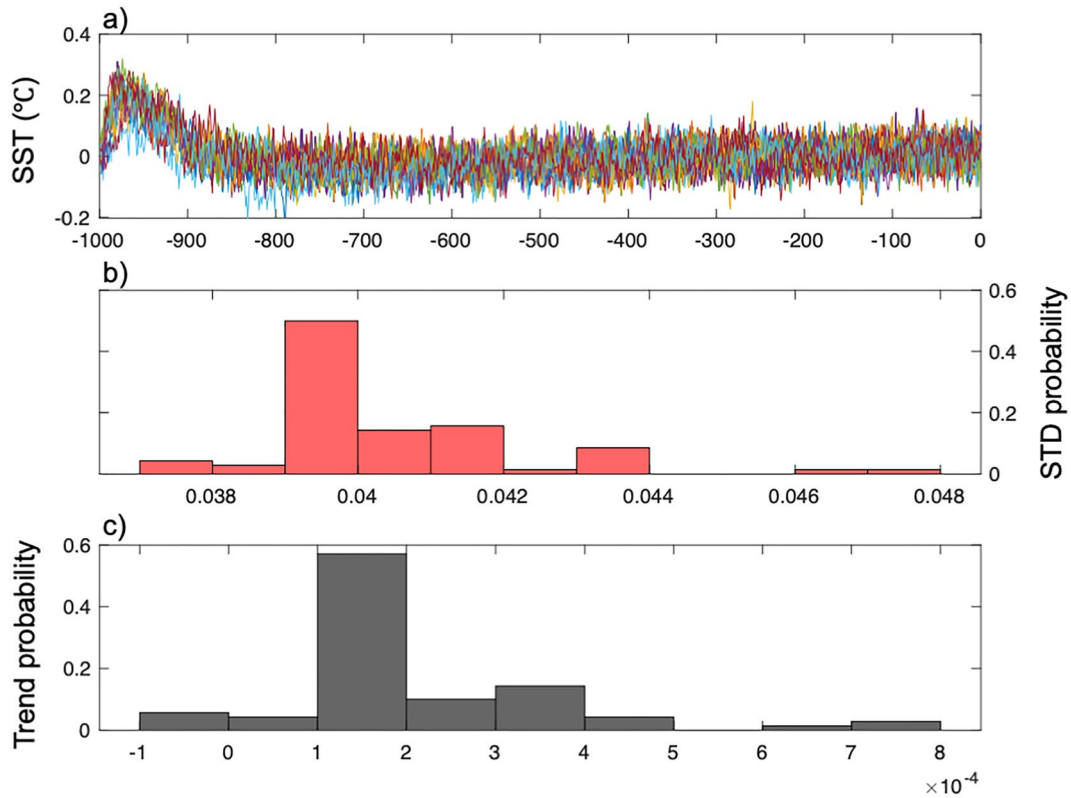

Figure 2. Global mean sea surface temperature anomalies (SST, unit: °C) in the spin-up period for ensemble members: (a) Time series (colors represent different members); (b) Probability of the standard deviations of the global mean sea surface temperatures lying within the bin ranges (non-dimensional); and (c) Probability of the trends of the binned global mean sea surface temperatures (non-dimensional). The time series is plotted from −999 to 0 model years, anomalies are computed relative to the base period of −500 to 0 model years, and the probabilities of the standard deviations and trends are computed from −500 to 0 model years.

(A. S. Gupta et al., 2013). This indicates that the LOVECLIM model is suitable for long-term transient experiments in paleoclimate research. The ensemble spread of the LOVECLIM-LCE simulation is defined by the standard deviation of the ensemble members (T. Liu et al., 2019).

All datasets are calculated as annual averages based on the arithmetic mean of the April–March time window. This is to avoid interruption of the growing season of trees in both the NH and Southern Hemisphere (SH), as 415 of 692 proxy records are from trees (ring width and density) (PAGES2k Consortium, 2017). The quantiles for the cumulative probabilities (5%, 50%, and 95%) of the proxy reconstruction ensembles and the climate model simulation ensembles were calculated for model–data comparison.

The AMOC index is defined as the maximum of the zonally averaged overturning stream function over the North Atlantic domain (30°–60°N) in the depth range from 500 m to 2,000 m according to the previous study (Liu et al., 2022). The northward heat transport index is the poleward heat transport in the North Atlantic at 35°N from an output variable (Northward Heat Transport, N_HEAT) in the CESM-LME simulation and (Meridional Heat Transport, MHT) in the LOVECLIM-LCE simulation.

2.3. Radiative Kernels

The radiative kernels are used to decompose the atmospheric radiative fluxes due to the radiative feedback including the Planck, lapse-rate, surface albedo, and water vapor feedbacks (Soden & Held, 2006). The radiative kernels method is defined by the formula as follows,

$$\lambda_{total} = \lambda_P + \lambda_L + \lambda_A + \lambda_W + \lambda_C \quad (1)$$

where the total feedback includes the Planck feedback (λ_P), lapse rate feedback (λ_L), surface albedo feedback (λ_A), water vapor feedback (λ_W), and cloud feedback (λ_C). These five feedbacks were determined by linearly regressing the surface air temperature change with each radiation flux (H. Wang et al., 2022). We used the monthly mean radiative kernels calculated with the CESM 1.1 model (Pendergrass et al., 2018). The input data include the surface air temperature at reference height, the atmospheric temperature, the specific humidity, the surface pressure, the net solar flux at the surface, the downwelling solar flux at the surface, the net longwave flux at the surface, the net solar flux at the top of the model, the net longwave flux at the top of the model, and these radiative fluxes are under clear-sky condition. The output data give the contribution of each feedback process to temperature change; the unit of the radiative feedback is W m^{-2} K^{-2}.

3. Results

Figure 3 shows the annual (April–March) temperature anomalies and differences between the RWP and LALIA in both model simulations and proxy data, including the probability (Figure 3a), and time evolution (Figure 3b), and spatial pattern (Figure 3c). The medians of the probabilities of the NH temperature changes between the RWP and LALIA, for both the LOVECLIM-LCE simulation and the proxy reconstruction, are larger than those of the SH, but the NH temperature changes between the RWP and LALIA in the CESM-past2k simulation are equivalent to those of the SH (Figure 3a). In addition, the CESM-past2k simulation has the largest temperature differences between the RWP and LALIA, and the proxy reconstruction has the smallest (Figure 3a).

The two simulated time series of NH and SH temperature anomalies are significantly related to the proxy reconstructions and the instrumental records (Figure 3b), but their means, amplitudes, and differences between data and models vary distinctly with the selected reference period (Figure S1 in Supporting Information S1). This indicates that the discrepancies of NH and SH temperature anomalies in the model–data comparison before the instrumental period are still evident if it is assumed that the current model simulations and the proxy reconstruction can broadly capture the instrumental hemispheric temperature variability. The other recent proxy reconstructions lie within the uncertainty of the PAGES2k hemispheric temperature reconstructions (Figure S2 in Supporting Information S1). This indicates that the PAGES2k temperature reconstructions are representative and robust. There are two distinct features in these NH reconstructions (Figure S2 in Supporting Information S1). One is that they show broadly consistent variability. This means that the multi-proxy reconstructions are dominated by the tree-ring reconstructions, and the tree-ring reconstructions are constrained by plenty of available overlapping tree-ring chronologies, which show a high correlation, especially in the second millennium of the CE and before the instrumental period. The other is that there are distinct differences in their means and amplitudes during the instrumental period. This means that the reconstruction methods have substantial influences on the calibration process, which is mostly calculated before ca. 1990 CE and does not include the rapid temperature increase of the last 30 years. Overall, it implies that the widely distributed tree-ring chronologies and the reconstruction methods adequately determine the NH temperature variability over the past two millennia.

Moreover, the gap between simulation and reconstruction is becoming smaller in more recent reconstructions (Figure S2 in Supporting Information S1), which is mainly reflected in the fact that the latest reconstructions can also show a clear response to the cooling events caused by volcanic eruptions. The amplitudes of cooling events in the latest tree-ring NH temperature reconstruction (Büntgen et al., 2021) (e.g., a NH volcanic eruption in 536 CE and a tropical volcanic eruption in 540 CE at the beginning of the LALIA) are even larger than the ensemble means of the simulations (Figure S2a in Supporting Information S1). There are apparent differences between the two reconstructions in the model–data comparison for SH temperature (Figures 3b2 and S2b). This means that proxy data with high resolution are still scarce, and they are critical to addressing the SH temperature variability over the past two millennia.

The spatial patterns of the differences between the RWP and LALIA in Figure 3c show that the areas of consistent warming are located at middle and high latitudes (45°–90°N) of the NH for the model–data results. There are significant temperature differences in Eurasia, North America, and the Arctic Ocean between the RWP and LALIA in the PAGES2k reconstructions (Figure 3c1). The LOVECLIM-LCE simulated temperature anomalies (Figure 3c2) confirm that the dominant temperature changes occur in the NH middle and high latitudes, where the response of the external forcing is larger than the spread of the internal variability. The CESM-past2k simulated temperature anomalies (Figure 3c3) also indicate warming in the middle and high latitudes of the NH. However,

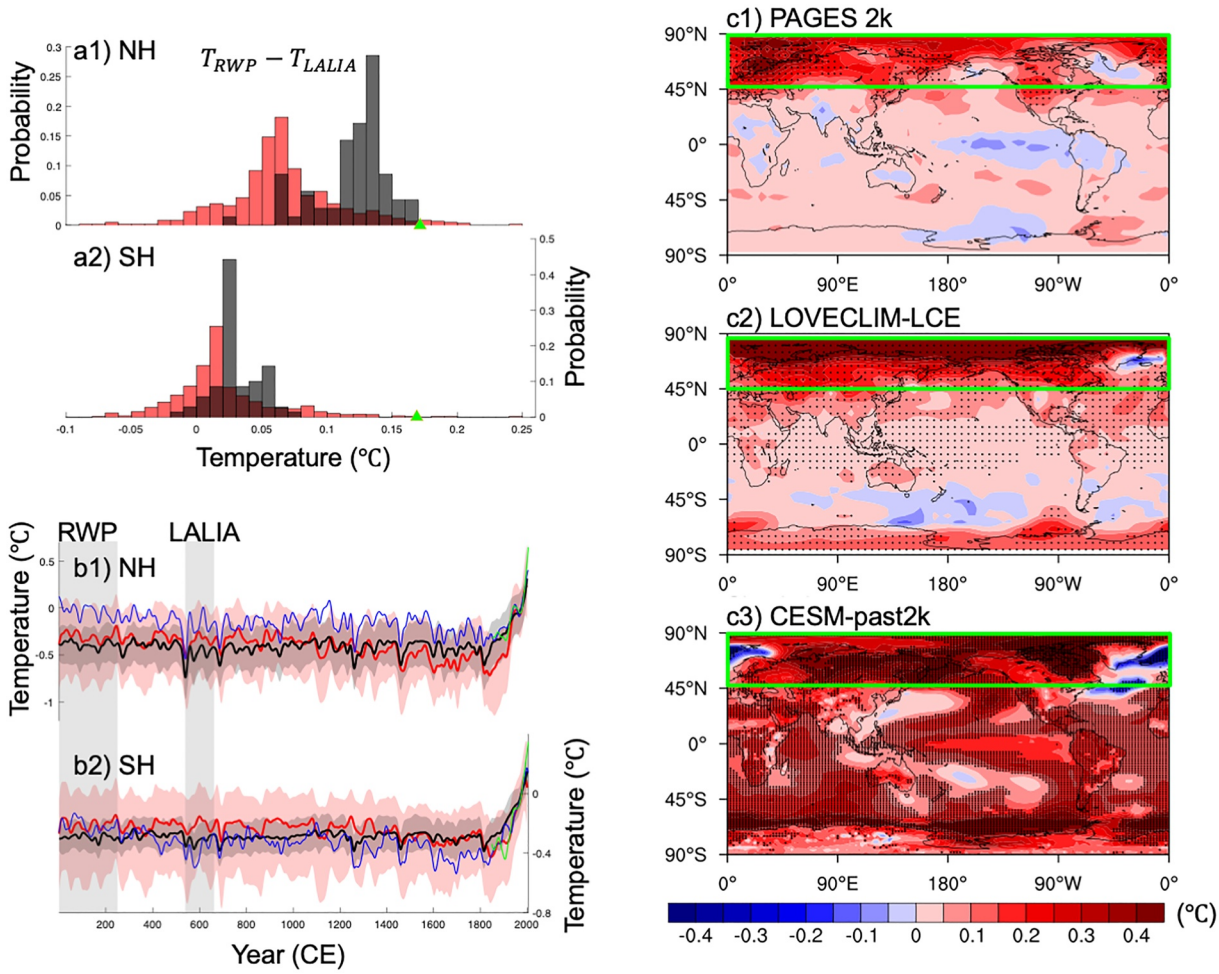

Figure 3. Comparison of model–data annual (April–March) temperature anomalies (unit: °C). (a) Probabilities of the NH (a1) and SH (a2) temperature differences [RWP (1–250 CE) minus LALIA (536–660 CE)] for the LOVECLIM-LCE ensemble simulations (black, non-dimensional) and the PAGES2k ensemble reconstructions (red, non-dimensional). Green triangles indicate the differences between the RWP and LALIA for the CESM-past2k simulation. (b) Median NH (b1) and SH (b2) temperature anomalies with 5%/95% percentiles for the LOVECLIM-LCE ensemble simulations (black) and the PAGES2k ensemble reconstructions (red). Blue lines denote the temperature anomalies for the CESM-past2k simulation, and green lines are the observed temperature anomalies for the HadCRUT4.5 observation dataset. Gray shaded bars indicate the RWP (1–250 CE) and LALIA (536–660 CE) periods. All data are smoothed by a 30-year Hamming filter. Anomalies are computed relative to the reference period of 1961–1990 CE. (c) Temperature field changes (RWP minus LALIA) for the PAGES2k ensemble reconstructions (c1), the LOVECLIM-LCE ensemble simulation (c2), and the CESM-past2k simulation (c3). Stippling indicates differences greater than the standard deviation of the ensemble members of the reconstruction (c1) and the LOVECLIM-LCE simulation (c2), and statistical significance of the CESM-past2k simulation (c3) at the 99% confidence level using Student's *t*-test. The green box represents the middle and high latitudes (45°–90°N) of the NH.

there are still apparent mismatches between model and proxy reconstruction. For example, strong warming in Antarctica is reflected in the two simulations (LOVECLIM-LCE and CESM-past2k) but is not present in the proxy reconstructions, and the proxy reconstructions show cold SST in the equatorial East Pacific that does not appear in the two simulations.

The model–data comparison of annual (April–March) precipitation anomalies is shown in Figure 4. The medians of the probabilities of precipitation changes between the RWP and LALIA, for both the LOVECLIM-LCE simulation and the PAGES2k proxy reconstruction, are distinctly higher in the NH than in the SH (Figure 4a), but the SH precipitation changes between the RWP and LALIA in the CESM-past2k simulation are slightly larger than those of the NH.

There are distinct discrepancies in the mean, amplitude, and trend of the annual mean precipitation anomalies in model–data comparison (Figure 4b). The LOVECLIM-LCE ensemble simulation outperforms the CESM-past2k simulation in terms of the time evolution of the NH annual mean precipitation anomalies (Figure 4b1). The NH

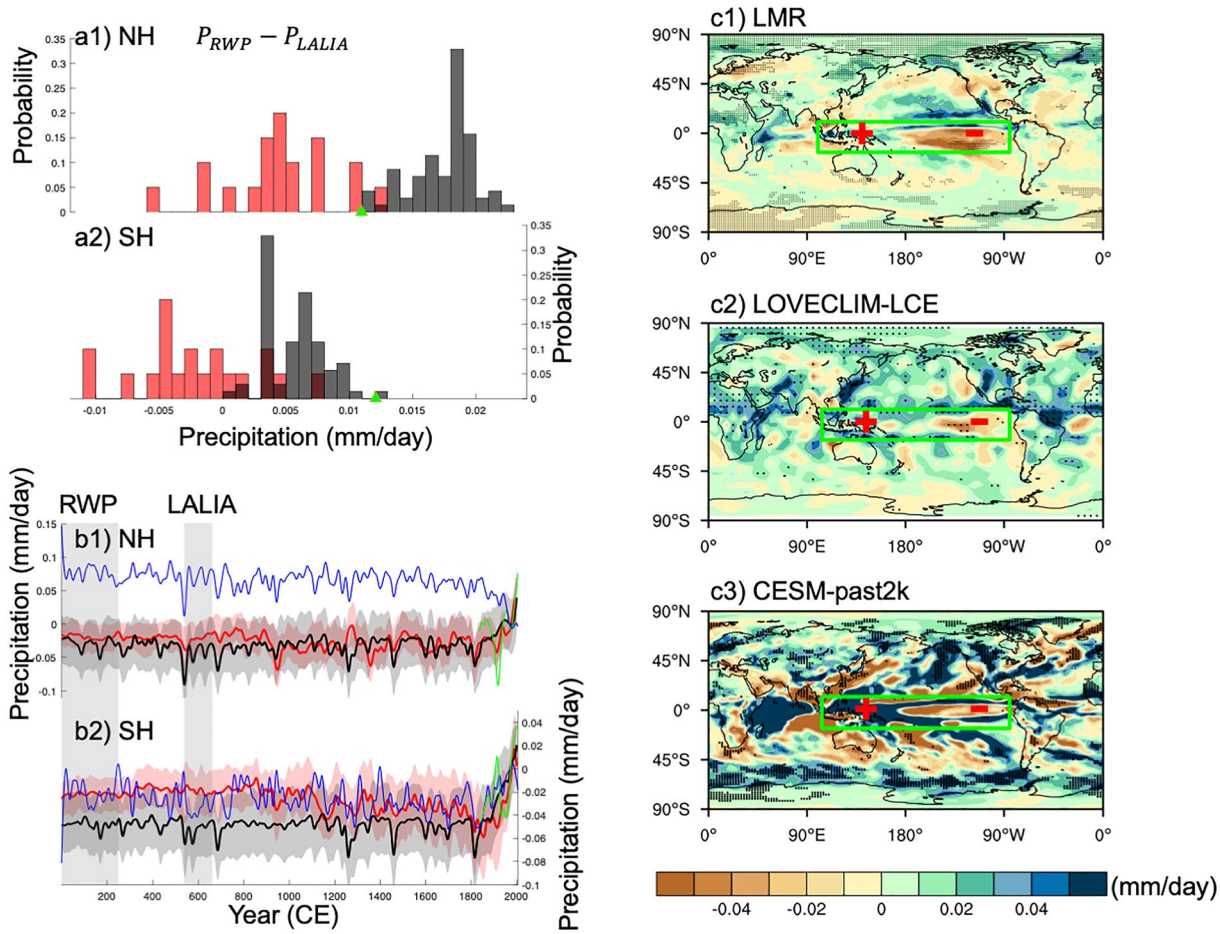

Figure 4. Annual (April–March) precipitation anomalies (unit: mm day^{-1}). (a) Probabilities of the NH (a1) and SH (a2) precipitation changes [RWP (1–250 CE) minus LALIA (536–660 CE)] for the LOVECLIM-LCE model (black, non-dimensional) and the LMR data (red, non-dimensional). Green triangles indicate the differences between the RWP and LALIA for the CESM-past2k simulation. (b) Median NH (b1) and SH (b2) precipitations with 5%/95% percentiles for model (black) and data (red). Blue lines denote the precipitation anomalies for the CESM-past2k simulation, and green lines are the precipitation anomalies for the 20CRv3 reanalysis dataset. Gray shaded bars indicate the RWP (1–250 CE) and LALIA (536–660 CE) periods. All data are smoothed by a 30-year Hamming filter. Anomalies are computed relative to the reference period 1961–1990 CE. (c) Precipitation field changes (RWP minus LALIA) for the data assimilation-based surface precipitation rate (c1), the LOVECLIM-LCE simulation (c2), and the CESM-past2k simulation (c3). Stippling indicates differences larger than the standard deviation of the ensemble members of the reconstruction (c1) and the LOVECLIM-LCE simulation (c2), and statistical significance of the CESM-past2k simulation (c3) at the 90% confidence level using Student's *t*-test. The green box represents the tropical Pacific (30°S–30°N, 90°–270°E). The symbols "+" and "–" represent an increase and decrease in the precipitation, respectively.

annual precipitation anomalies in the CESM-past2k simulation have an obvious false downward trend during the instrumental period (Figure 4b1). The selected reference period has a substantial influence on the precipitation comparison of the LMR data and the two simulations (Figure S3 in Supporting Information S1). The current model simulations and the proxy reconstruction seem not to capture the instrumental hemispheric precipitation variability (Figures 4b and S3).

The model–data precipitation comparisons all show low rainfall in the eastern equatorial Pacific and excess rainfall in the western equatorial Pacific (Figure 4c). The dominant features of the precipitation difference between the RWP and LALIA in the LMR data (Figure 4c1) are the decreased (increased) precipitation in the eastern (western) equatorial Pacific and the greater precipitation over most of the NH than over the SH. The dipole change of tropical Pacific precipitation is also seen in the LOVECLIM-LCE simulation (Figure 4c2), and the LOVECLIM-LCE simulation has more precipitation in the NH than the LMR data, especially in the global monsoon regions including the North American, West African, and Indian monsoons (Figure 4c2). The dipole change of tropical Pacific

precipitation is found in the CESM-past2k simulation (Figure 4c3), and the precipitation differences simulated by the CESM-past2k simulation are considerably larger than those of the LOVECLIM-LCE simulation (Figure 4c).

4. Discussion

Here we examine the factors responsible for the temperature differences between the RWP and LALIA periods. Two possible external forcings are considered: solar and volcanic. The solar activity difference between the RWP and LALIA is only 0.053 W m^{-2}, and this decreases to 0.013 W m^{-2} when the radiation reaches the top of the atmosphere. This would increase the mean global surface temperature by only ~0.0026°C using the algorithm in Nie et al. (2019). The volcanic forcing that reduces the mean global surface temperature in the LALIA by ~0.30°C relative to the RWP is 1.50 W m^{-2} greater in magnitude in the LALIA than the RWP, which is much larger than the influence of solar activity. Moreover, according to the latest dataset of volcanic stratospheric sulfur injections (evolo2k v3; Toohey & Sigl [2017]), the amount of sulfate injected into the stratosphere by volcanic eruptions during the RWP period was 58.75 Tg over 23 eruption events, whereas the corresponding values for the LALIA are 104.47 Tg (an increase of 77.82%) over just 15 eruption events. The radiation anomalies caused by different volcanic eruptions are proportional to the amount of sulfate injected into the stratosphere (Stenchikov et al., 2009). Thus, the temperature drop caused by eruptions during the LALIA period would be 70%–80% stronger than that during the RWP period if internal climate variability is ignored. From our results, we can infer that the dominant external forcing during the LALIA was more active volcanism compared with the RWP, which is consistent with the comparison between tree-ring records and the volcanic forcing reconstruction (Büntgen et al., 2016, 2020).

We conclude that the difference between the RWP and LALIA in the simulation is mainly induced by volcanic eruptions, the mechanism is that the cooling effect of the volcanic eruption during the LALIA is larger than that during the RWP. Note that there is no external forcing that can significantly increase the hemispheric temperature in the climate model, and only a possible major forcing (solar activity) contributes little to the temperature increase in the model (Schurer et al., 2014). Moreover, the other proxy records with low-resolution show some evident warming events over millennia and longer time frames (Jiang et al., 2021; Ljungqvist, 2010; Luterbacher et al., 2016; Tan et al., 2003; Wen et al., 2010; E. Zhang et al., 2019; C. Zhang et al., 2021), which are not in the climate model simulation (Shi et al., 2021). Therefore, we can infer that some positive feedback induced by solar activity may not be perfectly represented in the current models (Connolly et al., 2021; Matthes et al., 2017); for example, the cloud feedback (Zelinka et al., 2012) and the surface albedo feedback (H. Wang et al., 2022).

The stronger reduction in radiative forcing (more aerosol) during the LALIA gives an amplified cooling signal in the LALIA compared with the situation in the RWP. A quantitative analysis of radiative feedback for the CESM-past2k simulation is shown in Figures 5 and S4 in Supporting Information S1. We calculated the difference in feedback in the middle and high latitudes of the NH (45°–90°N) between the RWP and the LALIA. The largest feedback is the surface albedo feedback at 0.79 W m^{-2} K^{-1}, and the second most important feedback is the lapse-rate feedback at 0.64 W m^{-2} K^{-1}. The spatial patterns of the first two feedbacks show distinct positive feedbacks in the middle and high latitudes of the NH (Figure 5). This indicates that the surface albedo and lapse-rate feedbacks contribute most to stronger warming in the RWP in the middle and high latitudes of the NH, which is consistent with the recent analysis of polar amplification during the instrumental period (Hahn et al., 2021). The water vapor feedback also has a positive and substantial contribution in the middle and high latitudes of the NH of 0.58 W m^{-2} K^{-1}, but its spatial pattern shows that the major contributions appear in the tropics (Figure S4a in Supporting Information S1). The Planck feedback has a distinctly negative contribution (Figure S4b in Supporting Information S1), and the cloud feedback shows a complex and disordered pattern with 0.03 W m^{-2} K^{-1} in the middle and high latitudes of the NH (Figure S4c in Supporting Information S1).

The physical process of the first two dominant feedbacks (the surface albedo and the lapse rate feedbacks) is that the warming induced by the radiative forcing (because there is less volcanic aerosol in the stratosphere during the RWP) leads to the melting of snow and sea ice in high-latitude regions (Figure 6a2), which increases the amount of shortwave radiation absorbed at the surface, with the warming being further amplified by surface albedo feedback (Serreze & Francis, 2006; Winton, 2006). The LOVECLIM-LCE simulation cannot be used to calculate the radiative kernels, but the surface albedo anomaly also shows a distinct albedo–sea ice feedback (Figures 5b

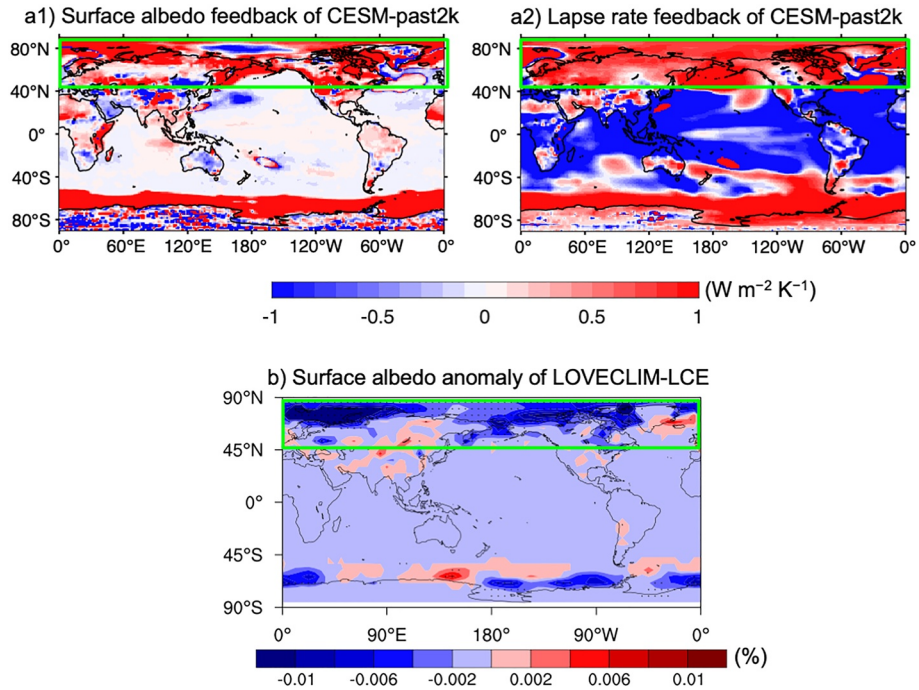

Figure 5. Radiative feedbacks. a1) Surface albedo feedback (unit: W m^{-2} K^{-1}) in the CESM-past2k simulation; a2) Lapse-rate feedback (unit: W m^{-2} K^{-1}) in the CESM-past2k simulation; (b) Surface albedo anomaly (RWP minus LALIA) (unit: %) in the LOVECLIM-LCE simulation. The green box represents the middle and high latitudes (45°–90°N) of the NH.

and 6a1). In addition, the cooling effect of the volcanic eruptions induces a positive lapse rate feedback through turbulent mixing of the vertical stratification of the atmosphere (Figure 5a2).

Moreover, we have calculated the upper ocean (0–700 m) heat content, Atlantic Meridional Overturning Circulation (AMOC), and the northward heat transport in North Atlantic in the two model simulations (Figures 6 and S5). The two climate model simulations (LOVECLIM-LCE and CESM-past2k) both show that the upper ocean heat content decreased rapidly and substantially after the larger-than-Pinatubo volcanic eruptions in the two hemispheres, which is consistent with other simulations (Brönnimann et al., 2019; Stenchikov et al., 2009). The upper-ocean heat content during the RWP period is distinctly larger than that of the LALIA period in the two hemispheres (Figures 6b and 6c). The recovery time of the upper ocean is relatively slow. The cumulative effect of multiple volcanic activities on ocean heat content partly explains the development of the RWP and LALIA periods and the hemispheric temperature variability over the centennial time scale.

Both climate model simulations show that the AMOC and the northward heat transport during the RWP period are significantly weaker than those of the LALIA period (Figure S5 in Supporting Information S1). This corresponds to the weaker AMOC during the CWP (Liu et al., 2020; Rahmstorf et al., 2015) and implies that the largest volcanic eruption makes a substantial contribution to the strong AMOC and the intense northward heat transport (Figure S5 in Supporting Information S1). However, this result does not support the coupled sea ice-ocean mechanism (Miller et al., 2012; Zhong et al., 2011), in which the decadally sequenced volcanic eruptions will lead to a weakened AMOC through expanded sea ice in the Arctic Ocean. Moreover, the amplitudes of the differences of the AMOC and the northward heat transport between the RWP and LALIA periods are distinctly smaller than that of the upper ocean heat content, and their small amplitudes cannot be used to explain the change in the upper ocean heat content. There was less Arctic sea ice during the RWP than during the LALIA, but there was no clear sea ice decrease in the Atlantic sector (Figure 6a). Thus, we assume that the upper ocean cooling response to the decreased short-wave radiative forcing is a dominant mechanism because the changes in the deep ocean can lead to delayed responses that accumulate between eruptions (Brönnimann et al., 2019; Church et al., 2005; M. Gupta & Marshall, 2018; Held et al., 2010). The reduced ocean heat content over centennial time scales due to the radiative feedbacks can be used to understand the warming over high-latitude regions of the NH in the RWP relative to the LALIA.

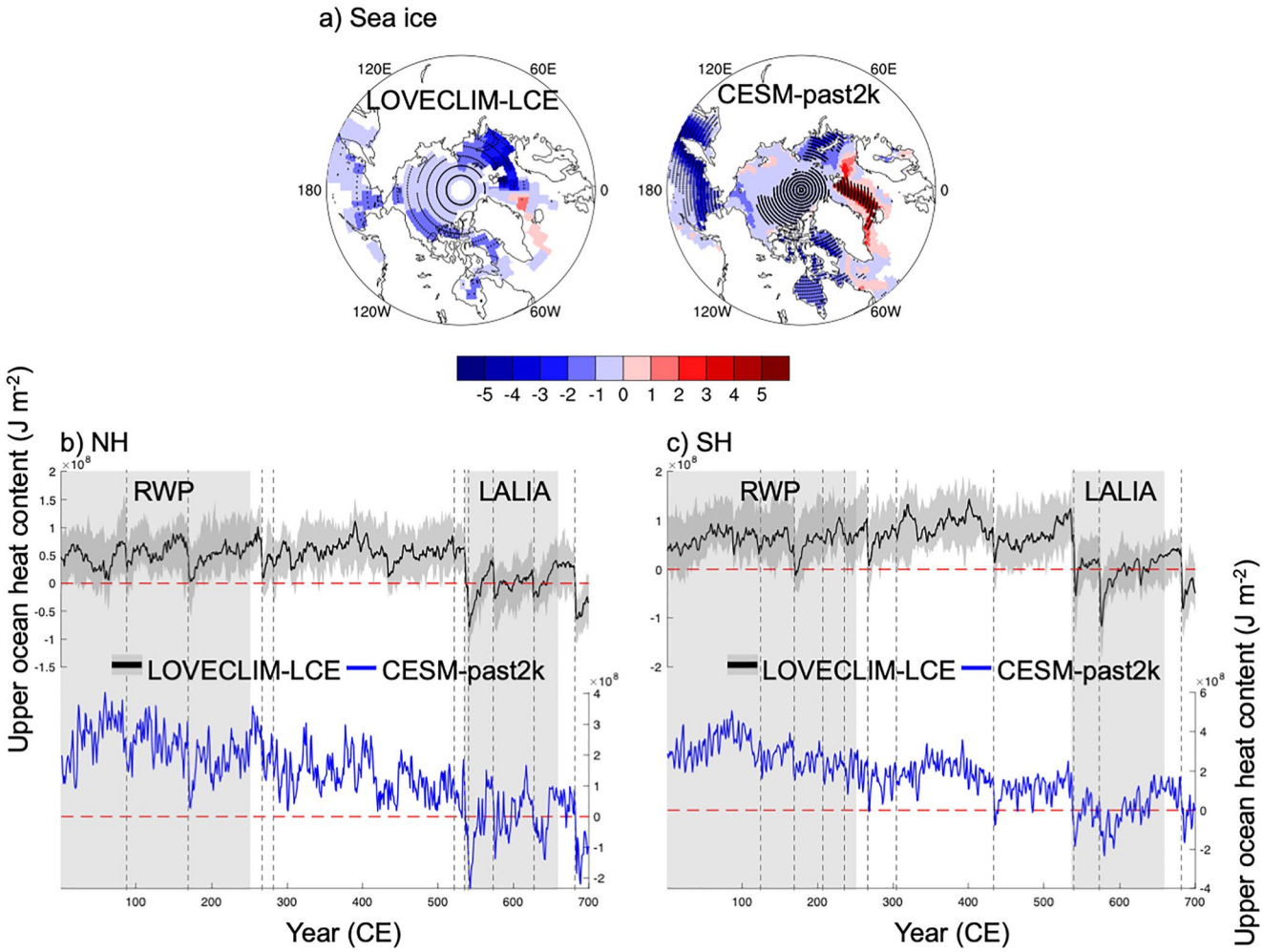

Figure 6. (a) Annual (April–March) sea ice (averaged lead area fraction (unit: %) changes [RWP (1–250 CE) minus LALIA (536–660 CE)] in the Arctic for the LOVECLIM-LCE simulation (a1), and the CESM-past2k simulation (a2). Stippling indicates differences larger than the standard deviation of the LOVECLIM-LCE simulation (a1), and statistical significance of the CESM-past2k simulation (a2) at the 90% confidence level using Student's *t*-test. (b) NH annual (April–March) upper ocean (0–700 m) heat content anomalies (unit: J m^{-2}) during the period 1–700 CE for the LOVECLIM-LCE simulation (b1), and the CESM-past2k simulation (b2). (c) SH annual (April–March) upper ocean (0–700 m) heat content anomalies (unit: J m^{-2}) during the period 1–700 CE for the LOVECLIM-LCE simulation (c1), and the CESM-past2k simulation (c2). Anomalies are computed relative to the LALIA. Black lines represent the larger eruptions than the 1991 CE Mount Pinatubo event, and dash red lines indicate zero line in (b) and (c). Gray shaded bars indicate the RWP (1–250 CE) and LALIA (536–660 CE) periods.

Here we consider the cause of the increased precipitation in the western Pacific and the decreased precipitation in the eastern Pacific during the RWP compared with the LALIA. The enhancement of the zonal circulation (Figure 7a) leads to the enhancement of the vertical velocity in the western Pacific in both model simulations and the increase of cloud cover in the CESM-past2k simulation (Figure 7b) that intercepts more longwave radiation (Figure 7c). The enhanced zonal circulation is coupled with the SST changes in the Pacific. The spatially varying component of SST changes indicates a role of internal variability, showing that the western Pacific is warmer than the eastern Pacific (Figure S6 in Supporting Information S1). The zonal gradient of SST is known to be coupled with the strength of zonal circulation, with enhanced (weakened) circulation corresponding to the strengthened (reduced) zonal gradient of SST. Previous studies have suggested several processes that may be involved in the coupling, including radiative feedback and ocean dynamic processes (Li et al., 2016; Sun et al., 2017). The changes in cloud cover and related longwave radiation (Figures 7c and 7d) support warmer SST in the western Pacific than in the eastern Pacific, which is consistent with the previous finding (Sun et al., 2017). This enhanced circulation also favors a precipitation pattern that is wet in the western Pacific and dry in the eastern Pacific (Figure 4c).

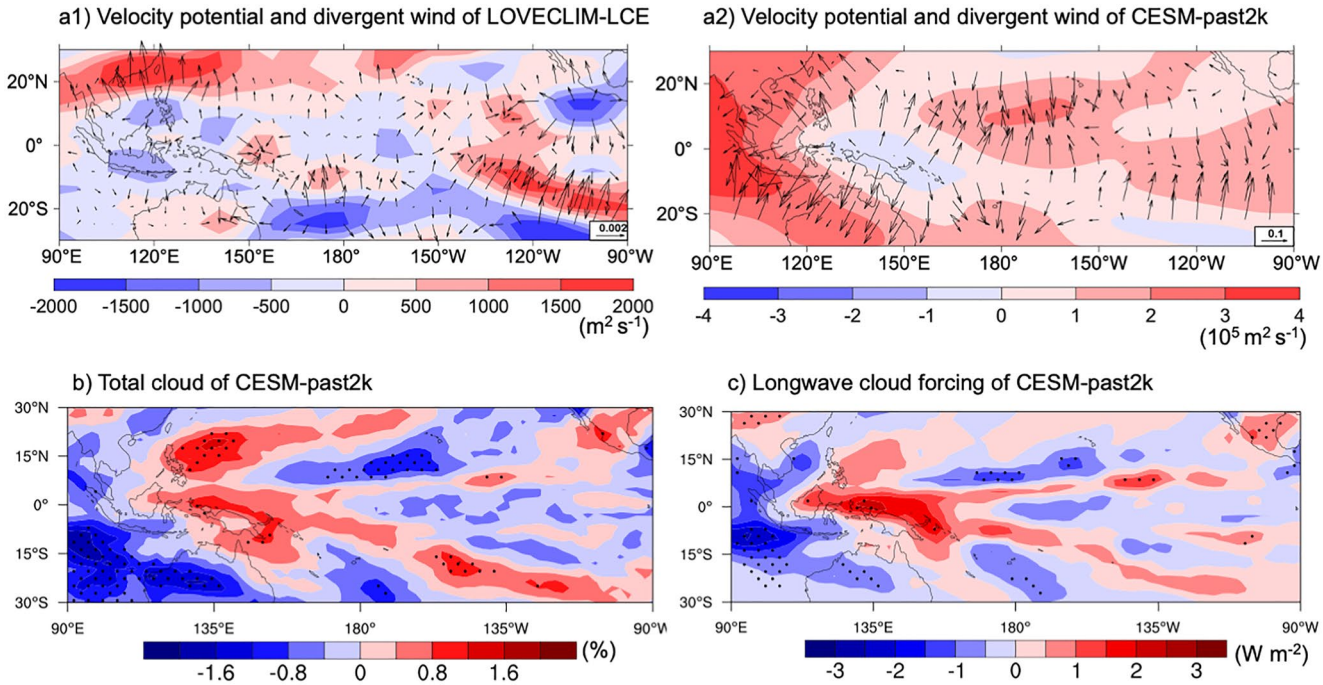

Figure 7. Responses of annual-mean (April–March) atmospheric circulation to the climate changes (RWP minus LALIA): (a) 200 hPa velocity potential (shading, units: $m^2\ s^{-1}$) and divergent wind (vectors, units: $m\ s^{-1}$) anomalies for the LOVECLIM-LCE (a1) and CESM-past2k (a2) simulations; (b) Vertically integrated total cloud fraction (units: %) for the CESM-past2k simulation; and (c) Longwave cloud forcing (units: $W\ m^{-2}$) for the CESM-past2k simulation. Stippling in (b) and (c) shows the 90% confidence level using Student's *t*-test.

There are two possible mechanisms that enhance zonal circulation: (a) The land–sea thermal contrast. The volcanic forcing could induce basin-scale SST simultaneous responses in both the Atlantic and Pacific in the same way, partly explaining the same-sign SST anomaly responses in the Atlantic and Pacific (Figure S6a in Supporting Information S1). We show the SST anomalies with the tropical Pacific mean removed from the SSTs to highlight the land–sea thermal contrast due to the Maritime Continent in the LOVECLIM-LCE simulation (Figure S6b1 in Supporting Information S1). This may strengthen the zonal circulation in the tropical Pacific. (b) The coupled air–sea inter-basin interaction. The spatially non-uniform feature of the tropical Pacific SST responses (Figure S6b in Supporting Information S1) can be explained by the "atmosphere–ocean bridge" mechanism (Gong et al., 2020; Sun et al., 2017). The velocity potential anomalies and the divergent wind show upper-level convergence over the eastern Pacific and divergence over the western Pacific in both model simulations, corresponding to a strengthened Pacific zonal circulation (Figure 7a). This is consistent with previous studies that showed that the zonal circulation in the Pacific has strengthened in response to warming in the Atlantic through the atmosphere–ocean bridge (Gong et al., 2020; Sun et al., 2017). The mechanism is that the SST is closely coupled to the atmospheric circulation changes in the Pacific. Climatologically, low-level clouds prevail over the eastern Pacific, whereas there are high-level clouds over the western Pacific. Thus, the decreased low-level cloud fraction (Figure 7b) associated with strengthened zonal circulation (Figure 7a) in the eastern Pacific could reduce longwave cloud forcing (Figure 7c) and precipitation. In the western Pacific, the high-level cloud increase (Figure 7b) in association with the zonal circulation changes (Figure 7a) could lead to more trapped longwave radiation (Figure 7c) and feedback to more precipitation.

5. Conclusions

We have used the LOVECLIM-LCE and CESM-past2k simulations to examine annual (April–March) climate differences between the RWP and LALIA. Large ensemble modeling shows that the climate difference between RWP and LALIA exceeds the spread of the internal variability of the climate system. The temperature difference is mainly in the warming in the middle and high latitudes of the NH during the RWP, and the precipitation differ-

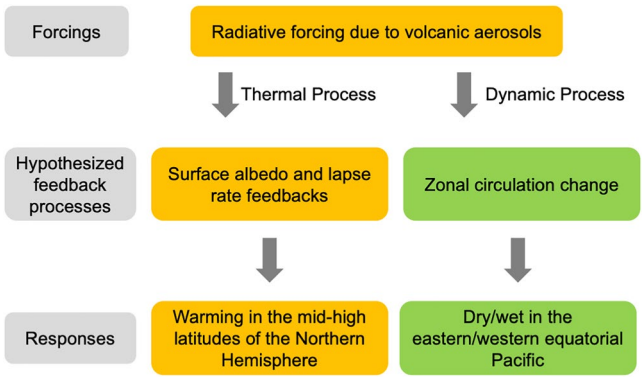

Figure 8. Schematic of the major processes that contributed to differences in annual temperature and precipitation anomalies in the NH between the RWP (1–250 CE) and LALIA (536–660 CE).

ence is mainly in the wetter western tropical Pacific and drier eastern tropical Pacific from the model–data comparison.

A higher frequency of volcanic eruptions during the LALIA is the main driver of the climate differences compared with the RWP. The temperature changes are further explained in terms of two radiative feedbacks (surface albedo and lapse-rate feedbacks). The decreased solar radiation caused by volcanic eruptions stimulates the positive sea ice–albedo feedback to sustain the expansion of the sea ice. In addition, the cooling effect of the volcanic eruptions induces positive lapse rate feedback through turbulent mixing of the vertical stratification of the atmosphere. The radiative feedback in the LALIA further reduce the ocean heat content over centennial time scales, whereas they amplify warming over high-latitude regions of the NH in the RWP (Figure 8).

The dynamics causing the precipitation changes are further explained by the atmosphere–ocean interaction. The land–sea thermal contrast in the tropical Pacific and the coupled air–sea inter-basin interaction increase the zonal east–west temperature gradient and strengthen the zonal circulation in the tropical Pacific. The zonal circulation change, combined with enhanced water vapor transport, causes dry (wet) conditions in the eastern (western) equatorial Pacific (Figure 8). Our simulation provides information to analyze climate mechanisms over the first millennium of the CE with greater certainty than previously found.

Conflict of Interest

The authors declare no conflicts of interest relevant to this study.

Data Availability Statement

The CESM-past2k model simulation is archived at the Climate Data Gateway on the NCAR website (https://www.earthsystemgrid.org/dataset/ucar.cgd.ccsm4.past2k_transient.html). The PAGES2k Global Common Era Multiproxy Temperature Field Reconstructions are archived in the NOAA data repository (https://www.ncdc.noaa.gov/paleo-search/study/26850). The other six reconstructions are archived in the NOAA data repository (Bün21, https://www.ncdc.noaa.gov/paleo/study/33215; Neu14, https://www.ncei.noaa.gov/pub/data/paleo/contributions_by_author/neukom2014/; Gui17, https://www.ncei.noaa.gov/access/paleo-search/study/21090; Sch15, https://www.ncdc.noaa.gov/paleo/study/18875; Wil16, https://www.ncdc.noaa.gov/paleo/study/19743). The codes of the kernels for the CESM model are freely available at https://github.com/apendergrass/cam5-kernels. The NH and SH temperature and precipitation data over the past 2,000 years from the LOVECLIM-LCE simulation (Figures 3b and 4b) are available at the World Data Center for Geophysics, Beijing (https://doi.org/10.12197/2022GA017).

Acknowledgments
We greatly appreciate the comments and suggestions of Hugues Goosse, Wei Liu, Huihong Xue, He Wang, and Lijuan Li. This work was jointly funded by the National Natural Science Foundation of China (Grant Nos. 41888101, 41877440, and 42077406), the Strategic Priority Research Program of the Chinese Academy of Sciences (Grant No. XDB26020000), and the Key Research Program of the Institute of Geology & Geophysics, CAS (Grant No. IGGCAS-201905). Feng Shi is funded by the Youth Innovation Promotion Association, CAS. Qiuzhen Yin is a Research Associate of Fonds de la Recherche Scientifique de Belgique (F.R.S-FNRS) and acknowledges the F.R.S.-FNRS funded grant MIS F.4529.18 for supporting her research. Computational resources were provided by the supercomputing facilities of the Université Catholique de Louvain (CISM/UCL) and the Consortium des Équipements de Calcul Intensif en Fédération Wallonie Bruxelles (CÉCI) funded by the F.R.S.-FNRS under convention 2.5020.11.

References

Berger, A. (1978). Long-term variations of daily insolation and quaternary climatic changes. *Journal of the Atmospheric Sciences*, *35*(12), 2362–2367. https://doi.org/10.1175/1520-0469(1978)035<2362:LTVODI>2.0.CO;2

Bianchi, G. G., & McCave, I. N. (1999). Holocene periodicity in North Atlantic climate and deep-ocean flow south of Iceland. *Nature*, *397*(6719), 515–517. https://doi.org/10.1038/17362

Brönnimann, S., Franke, J., Nussbaumer, S. U., Zumbühl, H. J., Steiner, D., Trachsel, M., et al. (2019). Last phase of the Little Ice Age forced by volcanic eruptions. *Nature Geoscience*, *12*, 650–656. https://doi.org/10.1038/s41561-019-0402-y

Büntgen, U., Allen, K., Anchukaitis, K. J., Arseneault, D., Boucher, É., Bräuning, A., et al. (2021). The influence of decision-making in tree ring-based climate reconstructions. *Nature Communications*, *12*, 3411. https://doi.org/10.1038/s41467-021-23627-6

Büntgen, U., Arseneault, D., Boucher, É., Churakova, O. V., Gennaretti, F., Crivellaro, A., et al. (2020). Prominent role of volcanism in Common Era climate variability and human history. *Dendrochronologia*, *64*, 125757. https://doi.org/10.1016/j.dendro.2020.125757

Büntgen, U., Myglan, V. S., Ljungqvist, F. C., McCormick, M., Di Cosmo, N., Sigl, M., et al. (2016). Cooling and societal change during the late Antique little ice age from 536 to around 660 AD. *Nature Geoscience*, *9*, 231–236. https://doi.org/10.1038/ngeo2652

Church, J. A., White, N. J., & Arblaster, J. M. (2005). Significant decadal-scale impact of volcanic eruptions on sea level and ocean heat content. *Nature*, *438*(7064), 74–77. https://doi.org/10.1038/nature04237

Connolly, R., Soon, W., Connolly, M., Baliunas, S., Berglund, J., Butler, C. J., et al. (2021). How much has the Sun influenced northern hemisphere temperature trends? An ongoing debate. *Research in Astronomy and Astrophysics*, *21*(6), 131. https://doi.org/10.1088/1674-4527/21/6/131

Crowley, T. J. (2000). Causes of climate change over the past 1000 years. *Science*, *289*(5477), 270–277. https://doi.org/10.1126/science.289.5477.270

Deser, C., Lehner, F., Rodgers, K., Ault, T., Delworth, T., DiNezio, P., et al. (2020). Insights from Earth system model initial-condition large ensembles and future prospects. *Nature Climate Change*, *10*, 277–286. https://doi.org/10.1038/s41558-020-0731-2

Deser, C., Phillips, A., Bourdette, V., & Teng, H. (2012). Uncertainty in climate change projections: The role of internal variability. *Climate Dynamics*, *38*(3–4), 527–546. https://doi.org/10.1007/s00382-010-0977-x

Foukal, P., Fröhlich, C., Spruit, H., & Wigley, T. (2006). Variations in solar luminosity and their effect on the Earth's climate. *Nature*, *443*(7108), 161–166. https://doi.org/10.1038/nature05072

Gao, C., Robock, A., & Ammann, C. (2008). Volcanic forcing of climate over the past 1500 years: An improved ice core-based index for climate models. *Journal of Geophysical Research: Atmospheres*, *113*, D23111. https://doi.org/10.1029/2008JD010239

Gong, Z., Sun, C., Li, J., Feng, J., Xie, F., Ding, R., et al. (2020). An inter-basin teleconnection from the North Atlantic to the subarctic North Pacific at multidecadal time scales. *Climate Dynamics*, *54*(1), 807–822. https://doi.org/10.1007/s00382-019-05031-5

Goosse, H., Brovkin, V., Fichefet, T., Haarsma, R., Huybrechts, P., Jongma, J., et al. (2010). Description of the Earth system model of intermediate complexity LOVECLIM version 1.2. *Geoscientific Model Development*, *3*(2), 603–633. https://doi.org/10.5194/gmd-3-603-2010

Goosse, H., Crespin, E., Dubinkina, S., Loutre, M.-F., Mann, M. E., Renssen, H., et al. (2012). The role of forcing and internal dynamics in explaining the "Medieval Climate Anomaly". *Climate Dynamics*, *39*(12), 2847–2866. https://doi.org/10.1007/s00382-012-1297-0

Goosse, H., Kay, J. E., Armour, K. C., Bodas-Salcedo, A., Chepfer, H., Docquier, D., et al. (2018). Quantifying climate feedbacks in polar regions. *Nature Communications*, *9*(1), 1919. https://doi.org/10.1038/s41467-018-04173-0

Goosse, H., Renssen, H., Timmermann, A., Bradley, R. S., & Mann, M. E. (2006). Using paleoclimate proxy-data to select optimal realisations in an ensemble of simulations of the climate of the past millennium. *Climate Dynamics*, *27*(2–3), 165–184. https://doi.org/10.1007/s00382-006-0128-6

Guillet, S., Corona, C., Stoffel, M., Khodri, M., Lavigne, F., Ortega, P., et al. (2017). Climate response to the Samalas volcanic eruption in 1257 revealed by proxy records. *Nature Geoscience*, *10*(2), 123–128. https://doi.org/10.1038/ngeo2875

Guion, A. (2017). *Evolution of surface temperature over the last 2000 years: Analysis of simulations performed by the climate model LOVECLIM 1.3. (Master Thesis)*. Université Catholique de Louvain. https://doi.org/10.13140/RG.2.2.22253.20965/2

Gupta, A. S., Jourdain, N. C., Brown, J. N., & Monselesan, D. (2013). Climate drift in the CMIP5 models. *Journal of Climate*, *26*(21), 8597–8615. https://doi.org/10.1175/JCLI-D-12-00521.1

Gupta, M., & Marshall, J. (2018). The climate response to multiple volcanic eruptions mediated by ocean heat uptake: Damping processes and accumulation potential. *Journal of Climate*, *31*(21), 8669–8687. https://doi.org/10.1175/JCLI-D-17-0703.1

Hahn, L. C., Armour, K. C., Zelinka, M. D., Bitz, C. M., & Donohoe, A. (2021). Contributions to polar amplification in CMIP5 and CMIP6 models. *Frontiers of Earth Science*, *9*(725). https://doi.org/10.3389/feart.2021.710036

Hegerl, G. C., Crowley, T. J., Baum, S. K., Kim, K. Y., & Hyde, W. T. (2003). Detection of volcanic, solar and greenhouse gas signals in paleo-reconstructions of Northern Hemispheric temperature. *Geophysical Research Letters*, *30*(5). https://doi.org/10.1029/2002GL016635

Helama, S., Jones, P. D., & Briffa, K. R. (2017). Dark ages cold period: A literature review and directions for future research. *The Holocene*, *27*(10), 1600–1606. https://doi.org/10.1177/0959683617693898

Held, I. M., Winton, M., Takahashi, K., Delworth, T., Zeng, F., & Vallis, G. K. (2010). Probing the fast and slow components of global warming by returning abruptly to preindustrial forcing. *Journal of Climate*, *23*(9), 2418–2427. https://doi.org/10.1175/2009JCLI3466.1

Jiang, L., Yu, K., Han, T., Tao, S., & Zhang, H. (2021). Coral perspective on temperature seasonality and interannual variability in the northern South China Sea during the Roman Warm Period. *Global and Planetary Change*, *207*, 103675. https://doi.org/10.1016/j.gloplacha.2021.103675

Jungclaus, J. H., Bard, E., Baroni, M., Braconnot, P., Cao, J., Chini, L. P., et al. (2017). The PMIP4 contribution to CMIP6-Part 3: The last millennium, scientific objective, and experimental design for the PMIP4 past1000 simulations. *Geoscientific Model Development*, *10*(11), 4005–4033. https://doi.org/10.5194/gmd-10-4005-2017

Keigwin, L. (1996). The little ice age and medieval warm period in the Sargasso Sea. *Science*, *274*(5292), 1503. https://doi.org/10.1126/science.274.5292.1504

Lawrence, D. M., Hurtt, G. C., Arneth, A., Brovkin, V., Calvin, K. V., Jones, A. D., et al. (2016). The land use model Intercomparison project (LUMIP) contribution to CMIP6: Rationale and experimental design. *Geoscientific Model Development*, *9*(9), 2973–2998. https://doi.org/10.5194/gmd-9-2973-2016

Li, X., Xie, S.-P., Gille, S. T., & Yoo, C. (2016). Atlantic-induced pan-tropical climate change over the past three decades. *Nature Climate Change*, *6*(3), 275–279. https://doi.org/10.1038/nclimate2840

Liu, T., Tang, Y., Yang, D., Cheng, Y., Song, X., Hou, Z., et al. (2019). The relationship among probabilistic, deterministic and potential skills in predicting the ENSO for the past 161 years. *Climate Dynamics*, *53*(11), 6947–6960. https://doi.org/10.1007/s00382-019-04967-y

Liu, W., Fedorov, A. V., Xie, S.-P., & Hu, S. (2020). Climate impacts of a weakened Atlantic Meridional overturning circulation in a warming climate. *Science Advances*, *6*(26), eaaz4876. https://doi.org/10.1126/sciadv.aaz4876

Liu, W., Shi, F., Xiao, G., Xue, H., Yin, Q., Liu, F., et al. (2022). Bidecadal temperature anomalies over the Tibetan Plateau and Arctic in response to the 1450s volcanic eruptions. *Journal of Geophysical Research: Atmospheres*, *127*, e2021JD035769. https://doi.org/10.1029/2021jd035769

Ljungqvist, F. C. (2010). A new reconstruction of temperature variability in the extra-tropical Northern Hemisphere during the last two millennia. *Geografiska Annaler: Physical Geography*, *92*(3), 339–351. https://doi.org/10.1111/j.1468-0459.2010.00399.x

Luterbacher, J., Werner, J. P., Smerdon, J. E., Fernández-Donado, L., González-Rouco, F. J., Barriopedro, D., et al. (2016). European summer temperatures since Roman times. *Environmental Research Letters*, *11*(2), 024001. https://doi.org/10.1088/1748-9326/11/2/024001

Matthes, K., Funke, B., Andersson, M. E., Barnard, L., Beer, J., Charbonneau, P., et al. (2017). Solar forcing for CMIP6 (v3.2). *Geoscientific Model Development*, *10*(6), 2247–2302. https://doi.org/10.5194/gmd-10-2247-2017

Meinshausen, M., Vogel, E., Nauels, A., Lorbacher, K., Meinshausen, N., Etheridge, D. M., et al. (2017). Historical greenhouse gas concentrations for climate modelling (CMIP6). *Geoscientific Model Development*, *10*(5), 2057–2116. https://doi.org/10.5194/gmd-10-2057-2017

Miller, G. H., Geirsdóttir, Á., Zhong, Y., Larsen, D. J., Otto-Bliesner, B. L., Holland, M. M., et al. (2012). Abrupt onset of the Little Ice Age triggered by volcanism and sustained by sea-ice/ocean feedbacks. *Geophysical Research Letters*, *39*(2). https://doi.org/10.1029/2011GL050168

Morice, C. P., Kennedy, J. J., Rayner, N. A., & Jones, P. D. (2012). Quantifying uncertainties in global and regional temperature change using an ensemble of observational estimates: The HadCRUT4 data set. *Journal of Geophysical Research: Atmospheres*, *117*(D8), D08101. https://doi.org/10.1029/2011JD017187

Neukom, R., Gergis, J., Karoly, D. J., Wanner, H., Curran, M., Elbert, J., et al. (2014). Inter-hemispheric temperature variability over the past millennium. *Nature Climate Change*, *4*, 362–367. https://doi.org/10.1038/nclimate2174

Neukom, R., Steiger, N., Gómez-Navarro, J. J., Wang, J., & Werner, J. P. (2019). No evidence for globally coherent warm and cold periods over the preindustrial Common Era. *Nature*, *571*(7766), 550–554. https://doi.org/10.1038/s41586-019-1401-2

Nie, Y., Li, L., Tang, Y., & Wang, B. (2019). Impacts of changes of external forcings from CMIP5 to CMIP6 on surface temperature in FGOALS-g2. *Scientific Online Letters on the Atmosphere*, *15*, 211–215. https://doi.org/10.2151/sola.2019-038

Otto-Bliesner, B. L., Brady, E. C., Fasullo, J., Jahn, A., Landrum, L., Stevenson, S., et al. (2016). Climate variability and change since 850 C.E.: An ensemble approach with the Community Earth system model (CESM). *Bulletin of the American Meteorological Society*, *97*, 735–754. https://doi.org/10.1175/BAMS-D-14-00233.1

PAGES2k Consortium. (2017). A global multiproxy database for temperature reconstructions of the Common Era. *Scientific Data*, *4*(170088). https://doi.org/10.1038/sdata.2017.88

Pendergrass, A. G., Conley, A., & Vitt, F. M. (2018). Surface and top-of-atmosphere radiative feedback kernels for CESM-CAM5. *Earth System Science Data*, *10*(1), 317–324. https://doi.org/10.5194/essd-10-317-2018

Previdi, M., Smith, K. L., & Polvani, L. M. (2021). Arctic amplification of climate change: A review of underlying mechanisms. *Environmental Research Letters*, *16*(9), 093003. https://doi.org/10.1088/1748-9326/ac1c29

Rahmstorf, S., Box, J. E., Feulner, G., Mann, M. E., Robinson, A., Rutherford, S., & Schaffernicht, E. J. (2015). Exceptional twentieth-century slowdown in Atlantic Ocean overturning circulation. *Nature Climate Change*, *5*(5), 475–480. https://doi.org/10.1038/nclimate2554

Robock, A. (2000). Volcanic eruptions and climate. *Reviews of Geophysics*, *38*(2), 191–219. https://doi.org/10.1029/1998RG000054

Schmidt, G., Jungclaus, J., Ammann, C., Bard, E., Braconnot, P., Crowley, T., et al. (2011). Climate forcing reconstructions for use in PMIP simulations of the last millennium (v1. 0). *Geoscientific Model Development*, *4*(1), 33–45. https://doi.org/10.5194/gmd-4-33-2011

Schneider, D. P., Ammann, C. M., Otto-Bliesner, B. L., & Kaufman, D. S. (2009). Climate response to large, high-latitude and low-latitude volcanic eruptions in the Community Climate System Model. *Journal of Geophysical Research: Atmospheres*, *114*(D15). https://doi.org/10.1029/2008JD011222

Schneider, L., Smerdon, J. E., Büntgen, U., Wilson, R. J. S., Myglan, V. S., Kirdyanov, A. V., & Esper, J. (2015). Revising midlatitude summer temperatures back to A.D. 600 based on a wood density network. *Geophysical Research Letters*, *42*(11), 4556–4562. https://doi.org/10.1002/2015GL063956

Schurer, A. P., Tett, S. F. B., & Hegerl, G. C. (2014). Small influence of solar variability on climate over the past millennium. *Nature Geoscience*, *7*(2), 104–108. https://doi.org/10.1038/ngeo2040

Serreze, M. C., & Francis, J. A. (2006). The Arctic amplification debate. *Climate Change*, *76*(3), 241–264. https://doi.org/10.1007/s10584-005-9017-y

Shi, F., Lu, H., Guo, Z., Yin, Q., Wu, H., Xu, C., et al. (2021). The position of the Current Warm Period in the context of the past 22,000 years of summer climate in China. *Geophysical Research Letters*, *48*(5), e2020GL091940. https://doi.org/10.1029/2020GL091940

Shi, F., Yang, B., Feng, J., Li, J., Yang, F., & Guo, Z. (2015). Reconstruction of the Northern Hemisphere annual temperature change over the common era derived from tree rings. *Quaternary Sciences*, *35*(5), 1051–1063. (In Chinese with English Abstract). Retrieved from http://en.igg-journals.cn/article/doi/10.11928/j.issn.1001-7410.2015.05.01

Slivinski, L. C., Compo, G. P., Whitaker, J. S., Sardeshmukh, P. D., Giese, B. S., McColl, C., et al. (2019). Towards a more reliable historical reanalysis: Improvements for version 3 of the Twentieth Century Reanalysis system. *Quarterly Journal of the Royal Meteorological Society*, *145*(724), 2876–2908. https://doi.org/10.1002/qj.3598

Soden, B. J., & Held, I. M. (2006). An assessment of climate feedbacks in coupled ocean–atmosphere models. *Journal of Climate*, *19*(14), 3354–3360. https://doi.org/10.1175/jcli3799.1

Stenchikov, G., Delworth, T. L., Ramaswamy, V., Stouffer, R. J., Wittenberg, A., & Zeng, F. (2009). Volcanic signals in oceans. *Journal of Geophysical Research: Atmospheres*, *114*(D16). https://doi.org/10.1029/2008JD011673

Sun, C., Kucharski, F., Li, J., Jin, F.-F., Kang, I.-S., & Ding, R. (2017). Western tropical Pacific multidecadal variability forced by the Atlantic multidecadal oscillation. *Nature Communications*, *8*(1). https://doi.org/10.1038/ncomms15998

Tan, M., Liu, T., Hou, J., Qin, X., Zhang, H., & Li, T. (2003). Cyclic rapid warming on centennial-scale revealed by a 2650-year stalagmite record of warm season temperature. *Geophysical Research Letters*, *30*(12), 1617–1620. https://doi.org/10.1029/2003GL017352

Tardif, R., Hakim, G. J., Perkins, W. A., Horlick, K. A., Erb, M. P., Emile-Geay, J., et al. (2019). Last millennium reanalysis with an expanded proxy database and seasonal proxy modeling. *Climate of the Past*, *15*(4), 1251–1273. https://doi.org/10.5194/cp-15-1251-2019

Toohey, M., Krüger, K., Sigl, M., Stordal, F., & Svensen, H. (2016). Climatic and societal impacts of a volcanic double event at the dawn of the Middle Ages. *Climate Change*, *136*(3), 401–412. https://doi.org/10.1007/s10584-016-1648-7

Toohey, M., & Sigl, M. (2016). Ice core-inferred volcanic stratospheric sulfur injection from 500 BCE to 1900 CE. World Data Center for Climate (WDCC) at DKRZ. https://doi.org/10.1594/WDCC/eVolv2k_v1

Toohey, M., & Sigl, M. (2017). Volcanic stratospheric sulfur injections and aerosol optical depth from 500 BCE to 1900 CE. *Earth System Science Data*, *9*(2), 809–831. https://doi.org/10.5194/essd-9-809-2017

Toohey, M., Stevens, B., Schmidt, H., & Timmreck, C. (2016). Easy volcanic aerosol (EVA v1.0): An idealized forcing generator for climate simulations. *Geoscientific Model Development*, *9*(11), 4049–4070. https://doi.org/10.5194/gmd-9-4049-2016

van Dijk, E., Jungclaus, J., Lorenz, S., Timmreck, C., & Krüger, K. (2022). Was there a volcanic-induced long-lasting cooling over the Northern Hemisphere in the mid-6th–7th century? *Climate of the Past*, *18*, 1601–1623. https://doi.org/10.5194/cp-18-1601-2022

Vieira, L. E. A., Solanki, S. K., Krivova, N. A., & Usoskin, I. (2011). Evolution of the solar irradiance during the Holocene. *Astronomy & Astrophysics*, *531*. https://doi.org/10.1051/0004-6361/201015843

Wang, H., Li, L., Chen, X., & Wang, B. (2022). Evaluating the nature and extent of changes to climate sensitivity between FGOALS-g2 and FGOALS-g3. *Journal of Geophysical Research: Atmospheres*, *127*(3), e2021JD035852. https://doi.org/10.1029/2021JD035852

Wang, T., Surge, D., & Walker, K. J. (2013). Seasonal climate change across the Roman Warm Period/Vandal Minimum transition using isotope sclerochronology in archaeological shells and otoliths, southwest Florida, USA. *Quaternary International*, *308–309*, 230–241. https://doi.org/10.1016/j.quaint.2012.11.013

Wang, Z., Li, Y., Liu, B., & Liu, J. (2015). Global climate internal variability in a 2000-year control simulation with Community Earth System Model (CESM). *Chinese Geographical Science*, *25*(3), 263–273. https://doi.org/10.1007/s11769-015-0754-1

Wen, R., Xiao, J., Chang, Z., Zhai, D., Xu, Q., Li, Y., & Itoh, S. (2010). Holocene precipitation and temperature variations in the East Asian monsoonal margin from pollen data from Hulun Lake in northeastern Inner Mongolia, China. *Boreas*, *39*(2), 262–272. https://doi.org/10.1111/j.1502-3885.2009.00125.x

Wilson, R., Anchukaitis, K., Briffa, K. R., Büntgen, U., Cook, E., D'Arrigo, R., et al. (2016). Last millennium northern hemisphere summer temperatures from tree rings: Part I: The long term context. *Quaternary Science Reviews*, *134*, 1–18. https://doi.org/10.1016/j.quascirev.2015.12.005

Winton, M. (2006). Amplified Arctic climate change: What does surface albedo feedback have to do with it? *Geophysical Research Letters*, *33*(3). https://doi.org/10.1029/2005GL025244

Yan, Q., Zhang, Z., Wang, H., & Jiang, D. (2015). Simulated warm periods of climate over China during the last two millennia: The Sui-Tang warm period versus the Song-Yuan warm period. *Journal of Geophysical Research: Atmospheres*, *120*(6), 2229–2241. https://doi.org/10.1002/2014JD022941

Zelinka, M. D., Klein, S. A., & Hartmann, D. L. (2012). Computing and partitioning cloud feedbacks using cloud property histograms. Part II: Attribution to changes in cloud amount, altitude, and optical depth. *Journal of Climate*, *25*(11), 3736–3754. https://doi.org/10.1175/JCLI-D-11-00249.1

Zhang, C., Zhao, C., Zhou, A., Zhang, H., Liu, W., Feng, X., et al. (2021). Quantification of temperature and precipitation changes in northern China during the "5000-year" Chinese History. *Quaternary Science Reviews*, *255*, 106819. https://doi.org/10.1016/j.quascirev.2021.106819

Zhang, E., Chang, J., Shulmeister, J., Langdon, P., Sun, W., Cao, Y., et al. (2019). Summer temperature fluctuations in Southwestern China during the end of the LGM and the last deglaciation. *Earth and Planetary Science Letters*, *509*, 78–87. https://doi.org/10.1016/j.epsl.2018.12.024

Zhang, M., Hack, J., Kiehl, J., & Cess, R. (1994). Diagnostic study of climate feedback processes in atmospheric general circulation models. *Journal of Geophysical Research: Atmospheres*, *99*(D3), 5525–5537. https://doi.org/10.1029/93JD03523

Zhong, Y., Jahn, A., Miller, G. H., & Geirsdottir, A. (2018). Asymmetric cooling of the Atlantic and Pacific Arctic during the past two millennia: A dual observation-modeling study. *Geophysical Research Letters*, *45*(22), 12497–12505. https://doi.org/10.1029/2018GL079447

Zhong, Y., Miller, G. H., Otto-Bliesner, B. L., Holland, M. M., Bailey, D. A., Schneider, D. P., & Geirsdottir, A. (2011). Centennial-scale climate change from decadally-paced explosive volcanism: A coupled sea ice-ocean mechanism. *Climate Dynamics*, *37*(11), 2373–2387. https://doi.org/10.1007/s00382-010-0967-z